

## SIZE DEPENDENT LARGE DISPLACEMENTS OF MICROBEAMS AND MICROFRAMES

Cong Ich Le<sup>1,\*</sup> , Dinh Kien Nguyen<sup>2,3</sup> 

<sup>1</sup>*Le Quy Don Technical University, 236 Hoang Quoc Viet, Hanoi, Vietnam*

<sup>2</sup>*Institute of Mechanics, VAST, 18 Hoang Quoc Viet, Hanoi, Vietnam*

<sup>3</sup>*Graduate University of Science and Technology, VAST, 18 Hoang Quoc Viet, Hanoi, Vietnam*

\*E-mail: [lecongich79@lqdtu.edu.vn](mailto:lecongich79@lqdtu.edu.vn)

Received: 29 May 2022 / Published online: 10 September 2022

**Abstract.** The size dependent large displacement behavior of planar microbeams and microframes is studied in this paper using a corotational beam element. To account for the size effect, the modified couple stress theory (MCST) is employed in conjunction with Euler-Bernoulli beam theory in deriving the internal force vector and the tangent stiffness matrix of the beam element. The Newton-Raphson based iterative procedure is used in combination with the arc-length method to solve the nonlinear equilibrium equation and to trace the equilibrium paths. Various microbeams and microframes are analyzed to show the influence of the size effect on the large deflection behavior of the microstructure. The obtained result reveals that the size effect plays an important role on the large deflection response, and the displacements of the structure are over estimated by ignoring the size effect. A parametric study is carried out to highlight the influence of the material length scale parameter on the large displacement behavior of the microbeams and microframes.

*Keywords:* micro beam and frame, size effect, corotational formulation, large displacement analysis.

### 1. INTRODUCTION

Microbeams and microframes whose characteristic sizes down to the order of micron have wide applications in micro-electro-mechanical systems (MEMS) [1, 2]. In such applications, the microbeams and microframes are buckled and often undergone the large deflections, and geometric nonlinearity is an important factor which should be taken into account in analysis of these microstructures. Investigations on buckling and nonlinear behavior of microbeams and microframes has been extensively reported in the literature.

In the early works [3–8], the classical beam theories which ignore the size effect have been employed by several authors in modeling nonlinear bending of microbeams. The von Kármán nonlinearity in the axial strain-displacement relationship is adopted to account for the geometric nonlinearity, and the deflections of the microcantilever subjected to electro-mechanical loads are computed by the shooting [3] or Galerkin [5–8] methods.

In order to model the small size effect of microstructures various higher-order continuum theories such as the strain gradient elasticity theory (SGET) [9, 10], the modified couple stress theory (MCST) [11] have been developed to accompany a length scale parameter in modeling the mechanical behavior of such structures. Using these higher-order continuum theories, investigations on nonlinear bending of microbeams and microframes taking into account the size effect have been carried recently. In this line of works, Mohammadi and Mahzoon [12] derived the governing equations for post-buckling analysis of Euler-Bernoulli microbeams subjected to the axial force and temperature rise. Both the SGET and the MCST were employed by the authors to model the size effect in the microbeams. Xia et al. [13] developed a new nonlinear beam model for static bending, post-buckling and free vibration analysis of microbeams by introducing a material length scale parameter. The authors show that the size effect is significant when the ratio of characteristic thickness to the material length scale parameter is approximately equal to one, but is diminishing with the increase of the ratio. Adopting the MCST and SGET, Asghari et al. [14, 15] presented the nonlinear Timoshenko microbeam models with the size effects. The influence of the size effect on the bending and free vibration of the microbeams was examined by the authors using the numerical and semi-analytical methods. The SGET was also employed by Ramezani [16] to develop the micro scale non-linear beam model for large amplitude vibration analysis of a Timoshenko microbeam. The numerical result reveals that the geometric nonlinearity plays an essential role on increasing the natural frequency of the beam with a large thickness-to-length ratio. Akgöz and Civalek [17, 18] employed the modified strain gradient theory to derive the governing differential equations for size-dependent buckling analysis of microbeams. The influence of the size effect on the buckling characteristics of the beams was investigated with the aid of the Navier solution technique. The shooting method was employed in conjunction with Newton–Raphson method by Wang et al. [19] to compute the nonlinear deflections and post-buckling paths of microscale Euler–Bernoulli beams subjected to mechanical and thermal loading. The MCST was also used by the authors to capture the small size effect of the beams. Ansari et al. [20, 21] employed the differential quadrature method and the MCST to study nonlinear bending, buckling and vibration of third-order shear deformable functionally graded microbeams. The results of the work reveal that the frequencies and critical buckling loads increase, but the nonlinear-to-linear frequency ratios as well as the deflections decrease by decreasing the thickness-to-material length scale ratio. A two-node total Lagrangian beam element using the fifth-order interpolation was Dadgar-Rad and Beheshti [22] for the geometrically nonlinear bending analysis of microbeams and microframes. The general form of Mindlin’s strain gradient theory was used to capture the size effects at micron scales and Newton–Raphson method was adopted to compute the deformation of the microbeams and microframes. Attia and Mohamed [23] investigated the thermal buckling and post-buckling of tapered bidirectional functionally graded microbeams. The governing equations were derived using the Reddy beam theory and they are solved by the differential quadrature method in conjunction with the iterative Newton–Raphson method. Numerical investigation in the work shows that the material microstructure length scale which modelled via the MCST leads to the higher critical temperature, but the lower deflection.

The von Kármán nonlinear assumption employed in conjunction with a fixed coordinate system in the above references enables to model microstructure with moderate deflections and rotations only. In practical circumstances, the microbeams and microframes can undergo large displacements and rotations, which requires special approach to analyze. The finite element method as a powerful tool in handling nonlinearities is adopted herein to study the size dependent large displacements of planar microbeams and microframes. To this end, a corotational beam element which enables to capture both the small size effect and the large displacements of the beams is formulated and used in the study. The element with six degrees of freedom is derived using Euler–Bernoulli beam theory and the MCST to capture the size effect at microscale. Using the derived beam element, equilibrium equation in the context of the finite element analysis is derived and solved by the Newton–Raphson based iterative procedure in conjunction with arc-length method. Numerical investigations are carried out to highlight the influence of the size effect on the large displacement behavior of the microbeams and microframes.

## 2. COROTATIONAL BEAM ELEMENT WITH SIZE EFFECT

A two-node corotational beam element for large deflection analysis of microbeams and microframes is formulated in this section. The element is derived on the basis of Euler-Bernoulli beam theory and the MCTS to account for the size effect.

### 2.1. Local and global relationship

A planar 2-node beam element with its kinematics in two coordinate systems, a local  $(\bar{x}, \bar{z})$  and a global  $(x, z)$  as depicted in Fig. 1 is considered. The element is initially inclined to the  $x$ -axis an angle  $\theta_0$ . The global system is fixed, while the local one continuously moves and rotates with the element during its deformation. The system  $(\bar{x}, \bar{z})$  is chosen such that the origin is at the node 1 and the  $\bar{x}$ -axis directs towards the node 2. In such a local system, the axial displacement at the node 1 and the transverse displacements at both the nodes 1 and 2 are always zero,  $\bar{u}_1 = \bar{w}_1 = \bar{w}_2 = 0$ . The element vector

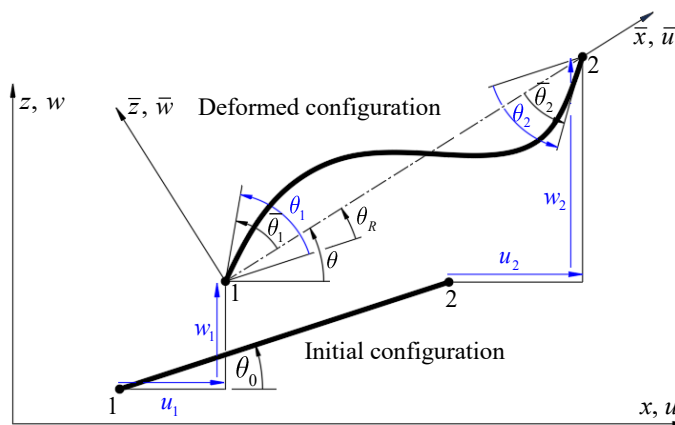


Fig. 1. A 2-node corotational beam element and its kinematics

of local nodal displacements, ( $\bar{\mathbf{d}}$ ), thus contains only three components

$$\bar{\mathbf{d}} = \{\bar{u}_2, \bar{\theta}_1, \bar{\theta}_2\}^T, \quad (1)$$

where  $\bar{u}_2$  is the local axial displacements at the node 2;  $\bar{\theta}_1$  and  $\bar{\theta}_2$  are the local rotations at the nodes 1 and 2, respectively. In Eq. (1) and hereafter, a superscript 'T' denotes the transpose of a vector or a matrix, and the bar suffix is used to indicate a variable with respect to the local system.

The global nodal displacements in general are nonzero, and the element vector of global nodal displacements ( $\mathbf{d}$ ) has six components as

$$\mathbf{d} = \{u_1, u_2, w_1, \theta_1, w_2, \theta_2\}^T, \quad (2)$$

where  $u_i, w_i, \theta_i$  ( $i = 1, 2$ ) are, respectively, the global axial, transverse displacements and rotation at the node  $i$ .

The vectors of nodal internal forces associated with the nodal displacements in Eqs. (1) and (2) are as follows

$$\begin{aligned} \bar{\mathbf{f}}_{in} &= \{\bar{f}_{\bar{u}}, \bar{\mathbf{f}}_{\bar{\theta}}\}^T, \quad \text{with } \bar{f}_{\bar{u}} = \bar{N}_2, \quad \bar{\mathbf{f}}_{\bar{\theta}} = \{\bar{M}_1, \bar{M}_2\}^T, \\ \mathbf{f}_{in} &= \{\mathbf{f}_u, \mathbf{f}_{\theta}\}^T, \quad \text{with } \mathbf{f}_u = \{N_1, N_2\}^T, \quad \mathbf{f}_{\theta} = \{Q_1, M_1, Q_2, M_2\}^T. \end{aligned} \quad (3)$$

In the above equation,  $N_i, Q_i$  and  $M_i$  ( $i = 1, 2$ ) are, respectively, the global nodal axial, shear forces and moments at nodes 1 and 2, and similar definition is applied for the local nodal forces and moments.

The local displacement and rotations in Eq. (1) are related to the global ones in Eq. (2) can be obtained from geometric consideration of Fig. 1 as

$$\bar{u}_2 = l_c - l_o, \quad \bar{\theta}_1 = \theta_1 - \theta_R, \quad \bar{\theta}_2 = \theta_2 - \theta_R. \quad (4)$$

In the above equation,  $l_o$  and  $l_c$  are, respectively, the initial and current element lengths, which can be computed from the element coordinates and current nodal displacements; The element rigid rotation  $\theta_R$  is calculated as [24,25]

$$\theta_R = \theta - \theta_0, \quad \text{with } \theta = \arctan\left(\frac{Z_2 - Z_1}{X_2 - X_1}\right), \quad (5)$$

with  $(X_i, Z_i)$  ( $i = 1, 2$ ) are the current global coordinates of the node  $i$ .

Assuming the strain energy ( $U$ ) of the element has been derived, the global nodal force vector  $\mathbf{f}_{in}$  and the tangent stiffness matrix  $\mathbf{k}_t$  for the element can be obtained by successive differentiating  $U$  with respect to the global vector of nodal displacements as

$$\mathbf{f}_{in} = \frac{\partial U}{\partial \mathbf{d}} = \frac{\partial U}{\partial \bar{\mathbf{d}}} \frac{\partial \bar{\mathbf{d}}}{\partial \mathbf{d}} = \mathbf{T}_1^T \bar{\mathbf{f}}_{in}, \quad \mathbf{k}_t = \frac{\partial^2 U}{\partial \mathbf{d}^2} = \mathbf{T}_1^T \bar{\mathbf{k}}_t \mathbf{T}_1 + \bar{N}_2 \mathbf{T}_2 + (\bar{M}_1 + \bar{M}_2) \mathbf{T}_3. \quad (6)$$

In the above equations,  $\bar{\mathbf{f}}_{in} = \partial U / \partial \bar{\mathbf{d}}$  and  $\bar{\mathbf{k}}_t = \partial^2 U / \partial \bar{\mathbf{d}}^2$  are, respectively, the local nodal force vector and tangent stiffness matrix;  $\mathbf{T}_1, \mathbf{T}_2$  and  $\mathbf{T}_3$  are the transformation matrices, which can be computed from Eq. (4) as

$$\mathbf{T}_1 = \frac{\partial \bar{\mathbf{d}}}{\partial \mathbf{d}}, \quad \mathbf{T}_2 = \frac{\partial^2 \bar{u}_2}{\partial \mathbf{d}^2}, \quad \mathbf{T}_3 = -\frac{\partial^2 \theta_R}{\partial \mathbf{d}^2}. \quad (7)$$

Eqs. (6) and (7) completely define the element formulation provided that the local nodal force vector and tangent stiffness matrix are known.

## 2.2. Local formulations

Based on Euler–Bernoulli beam theory, the local displacements  $\bar{u}$  and  $\bar{w}$  of a point in the element in the  $\bar{x}$ - and  $\bar{z}$ -directions, respectively, are given by

$$\bar{u}(\bar{x}, \bar{z}) = \bar{u}_0(\bar{x}) - \bar{z}\bar{\theta}(\bar{x}), \quad \bar{w}(\bar{x}, \bar{z}) = \bar{w}_0(\bar{x}), \quad (8)$$

where  $\bar{u}_0(\bar{x})$  and  $\bar{w}_0(\bar{x})$  are, respectively, the axial and the transverse displacement of a point on the  $\bar{x}$ -axis, and  $\bar{\theta} = \partial\bar{w}_0/\partial\bar{x}$  is the local cross-sectional rotation.

A shallow arch expression for the local axial strain can be adopted for the large displacement analysis as [24]

$$\bar{\varepsilon}_x(\bar{x}, \bar{z}) = \bar{u}_{0,\bar{x}}(\bar{x}) + \frac{1}{2}\bar{w}_{0,\bar{x}}^2(\bar{x}) - \bar{z}\bar{\theta}_{,\bar{x}}(\bar{x}) = \bar{\varepsilon}_0(\bar{x}) - \bar{z}\bar{w}_{0,\bar{x}\bar{x}}(\bar{x}), \quad (9)$$

with  $\bar{\varepsilon}_0(\bar{x}) = \bar{u}_{0,\bar{x}}(\bar{x}) + \frac{1}{2}\bar{w}_{0,\bar{x}}^2(\bar{x})$  is the membrane strain. In Eq. (9) and hereafter, a subscript comma is used to denote the derivative with respect to the followed variable, e.g.  $\bar{w}_{0,\bar{x}} = \partial\bar{w}_0/\partial\bar{x}$ .

Assuming the linearly elastic behavior for the element material, the axial stress ( $\bar{\sigma}_x$ ) is related to the axial strain (9) by

$$\bar{\sigma}_x(\bar{x}, \bar{z}) = E\bar{\varepsilon}_x(\bar{x}, \bar{z}) = E(\bar{\varepsilon}_0 - \bar{z}\bar{w}_{0,\bar{x}\bar{x}}), \quad (10)$$

where  $E$  is Young's modulus.

Interpolations are necessary to introduce for the local displacements. Here, the linear function and Hermite cubic polynomials are respectively used for  $\bar{u}_0$  and  $\bar{w}_0$  as

$$\bar{u}_0 = h_{\bar{u}}\bar{u}_2, \quad \bar{w}_0 = \mathbf{h}_{\bar{w}}\bar{\boldsymbol{\theta}}, \quad (11)$$

where  $\bar{\boldsymbol{\theta}} = \{\bar{\theta}_1, \bar{\theta}_2\}^T$ , and

$$h_{\bar{u}} = \frac{\bar{x}}{l_o}, \quad \mathbf{h}_{\bar{w}} = \left\{ \bar{x} - \frac{2\bar{x}^2}{l_o} + \frac{\bar{x}^3}{l_o^2}, \quad -\frac{\bar{x}^2}{l_o} + \frac{\bar{x}^3}{l_o^2} \right\}. \quad (12)$$

Eqs. (11) and (12) have been written by using  $\bar{u}_1 = \bar{w}_1 = \bar{w}_2 = 0$ . Differentiating  $\bar{u}_0$  and  $\bar{w}_0$  in (11) with respect to  $\bar{x}$  gives

$$\bar{u}_{0,\bar{x}} = b_{\bar{u}}\bar{u}_2, \quad \bar{w}_{0,\bar{x}} = \mathbf{b}_{\bar{w}}\bar{\boldsymbol{\theta}}, \quad \bar{w}_{0,\bar{x}\bar{x}} = \mathbf{c}_{\bar{w}}\bar{\boldsymbol{\theta}}, \quad (13)$$

with

$$b_{\bar{u}} = h_{\bar{u},\bar{x}} = \frac{1}{l_o}, \quad \mathbf{b}_{\bar{w}} = \mathbf{h}_{\bar{w},\bar{x}} = \left\{ 1 - \frac{4\bar{x}}{l_o} + \frac{3\bar{x}^2}{l_o^2}, \quad -\frac{2\bar{x}}{l_o} + \frac{3\bar{x}^2}{l_o^2} \right\}, \quad (14)$$

$$\mathbf{c}_{\bar{w}} = \mathbf{h}_{\bar{w},\bar{x}\bar{x}} = \left\{ -\frac{4}{l_o} + \frac{6\bar{x}}{l_o^2}, \quad -\frac{2}{l_o} + \frac{6\bar{x}}{l_o^2} \right\}.$$

The axial strain as given by Eq. (9) and the interpolating functions (12) cannot be used directly to generate a finite element formulation due to the membrane locking effect. In

order to avoid this problem, the membrane strain  $\bar{\varepsilon}_0$  in Eq. (11) is replaced by an effective strain defined as [24]

$$\bar{\varepsilon}_{\text{eff.}} = \frac{1}{l_0} \int_0^{l_0} \bar{\varepsilon}_0 d\bar{x} = \frac{1}{l_0} \int_0^{l_0} \left( \bar{u}_{0,\bar{x}} + \frac{1}{2} \bar{w}_{0,\bar{x}}^2 \right) d\bar{x}. \quad (15)$$

Using Eqs. (11), (12) and (13), one can write Eq. (15) in the form

$$\bar{\varepsilon}_{\text{eff.}} = b_{\bar{u}} \bar{u}_2 + \frac{1}{2l_0} \bar{\boldsymbol{\theta}}^T \int_0^{l_0} \mathbf{b}_{\bar{w}} \mathbf{b}_{\bar{w}}^T d\bar{x} \quad \bar{\boldsymbol{\theta}} = b_{\bar{u}} \bar{u}_2 + \bar{\boldsymbol{\theta}}^T \mathbf{B} \bar{\boldsymbol{\theta}}, \quad (16)$$

with

$$\mathbf{B} = \frac{1}{2l_0} \int_0^{l_0} \mathbf{b}_{\bar{w}} \mathbf{b}_{\bar{w}}^T d\bar{x} = \frac{1}{60} \begin{bmatrix} 4 & -1 \\ -1 & 4 \end{bmatrix}. \quad (17)$$

Since the classical continuum mechanics is not sufficient to predict the size-dependent behavior of micron-scale structures, the MCST proposed by Yang et al. [11] is adopted herein to evaluate the strain energy of the microbeam element as

$$U = \frac{1}{2} \int_V (\bar{\boldsymbol{\sigma}} : \bar{\boldsymbol{\varepsilon}} + \bar{\mathbf{m}} : \bar{\boldsymbol{\chi}}) dV, \quad (18)$$

where  $V$  is the element volume;  $\bar{\boldsymbol{\sigma}}$  and  $\bar{\boldsymbol{\varepsilon}}$  are, respectively, the stress and strain tensors;  $\bar{\mathbf{m}}$  is the deviatoric part of the couple stress tensor and  $\bar{\boldsymbol{\chi}}$  is the symmetric curvature tensor. The expressions for these tensors are as follows [11]

$$\bar{\boldsymbol{\sigma}} = \alpha \text{tr}(\bar{\boldsymbol{\varepsilon}}) \mathbf{I} + 2G \bar{\boldsymbol{\varepsilon}}, \quad \bar{\boldsymbol{\varepsilon}} = \frac{1}{2} [\nabla \bar{\mathbf{u}} + (\nabla \bar{\mathbf{u}})^T], \quad \bar{\boldsymbol{\chi}} = \frac{1}{2} [\nabla \bar{\boldsymbol{\beta}} + (\nabla \bar{\boldsymbol{\beta}})^T], \quad \bar{\mathbf{m}} = 2l^2 G \bar{\boldsymbol{\chi}}, \quad (19)$$

with  $\alpha$  and  $G$  are Lámé's constants,  $G = \frac{E}{2(1+\nu)}$  is the shear modulus;  $l$  is the material length scale parameter,  $\bar{\boldsymbol{\beta}}$  and  $\bar{\mathbf{u}}$  are, corresponding, the rotation vector and the displacement vector, that can be expressed as

$$\bar{\boldsymbol{\beta}} = \frac{1}{2} \text{curl}(\bar{\mathbf{u}}), \quad \bar{\mathbf{u}} = \{\bar{u}, 0, \bar{w}\}^T. \quad (20)$$

For the Euler–Bernoulli microbeam considered herein, the components of the rotation vector in Eq. (20) is

$$\bar{\boldsymbol{\beta}} = \{0, -\bar{w}_{0,\bar{x}}, 0\}^T. \quad (21)$$

Substituting (21) into expressions of  $\bar{\boldsymbol{\chi}}$  and  $\bar{\mathbf{m}}$  in Eq. (19) one gets

$$\bar{\boldsymbol{\chi}} = \begin{bmatrix} 0 & \bar{\chi}_{\bar{x}\bar{y}} & 0 \\ \bar{\chi}_{\bar{x}\bar{y}} & 0 & 0 \\ 0 & 0 & 0 \end{bmatrix} = \begin{bmatrix} 0 & -\frac{\bar{w}_{0,\bar{x}\bar{x}}}{2} & 0 \\ -\frac{\bar{w}_{0,\bar{x}\bar{x}}}{2} & 0 & 0 \\ 0 & 0 & 0 \end{bmatrix}, \quad (22)$$

$$\bar{\mathbf{m}} = 2l^2 G \bar{\boldsymbol{\chi}} = 2l^2 G \begin{bmatrix} 0 & -\frac{\bar{w}_{0,\bar{x}\bar{x}}}{2} & 0 \\ -\frac{\bar{w}_{0,\bar{x}\bar{x}}}{2} & 0 & 0 \\ 0 & 0 & 0 \end{bmatrix}.$$

In addition, the stress and strain tensors for the Euler-Bernoulli beam have the following simple forms

$$\bar{\boldsymbol{\sigma}} = \begin{bmatrix} \bar{\sigma}_{\bar{x}} & 0 & 0 \\ 0 & 0 & 0 \\ 0 & 0 & 0 \end{bmatrix}, \quad \bar{\boldsymbol{\varepsilon}} = \begin{bmatrix} \bar{\varepsilon}_{\bar{x}} & 0 & 0 \\ 0 & 0 & 0 \\ 0 & 0 & 0 \end{bmatrix}. \quad (23)$$

Using (22) and Eqs. (23), one can rewrite the strain energy for the element in Eq. (18) in the form

$$U = \frac{b}{2} \int_0^{l_0} \int_{-h/2}^{h/2} (\bar{\sigma}_{\bar{x}} \bar{\varepsilon}_{\bar{x}} + 2\bar{m}_{\bar{x}\bar{y}} \bar{\chi}_{\bar{x}\bar{y}}) dz dx. \quad (24)$$

Substituting Eqs. (9)–(16) and (22) into Eq. (24), one gets

$$U = \frac{1}{2} \int_0^{l_0} \left[ EA \left( (\bar{\boldsymbol{\theta}}^T \mathbf{B} \bar{\boldsymbol{\theta}})^2 + 2(\bar{\boldsymbol{\theta}}^T \mathbf{B} \bar{\boldsymbol{\theta}}) (b_{\bar{u}} \bar{u}_2) + (b_{\bar{u}} \bar{u}_2)^2 \right) + EI (\mathbf{c}_{\bar{w}} \bar{\boldsymbol{\theta}})^2 + GA l^2 (\mathbf{c}_{\bar{w}} \bar{\boldsymbol{\theta}})^2 \right] d\bar{x}. \quad (25)$$

The local internal force vector  $\bar{\mathbf{f}}_{in}$  is obtained by differentiating the strain energy (25) with respect to the local nodal displacements as

$$\begin{aligned} \bar{f}_{\bar{u}} &= \frac{\partial U}{\partial \bar{u}_2} = \int_0^{l_0} EA b_{\bar{u}} (\bar{\boldsymbol{\theta}}^T \mathbf{B} \bar{\boldsymbol{\theta}} + b_{\bar{u}} \bar{u}_2) d\bar{x} = EA (\bar{\boldsymbol{\theta}}^T \mathbf{B} \bar{\boldsymbol{\theta}} + b_{\bar{u}} \bar{u}_2), \\ \bar{\mathbf{f}}_{\bar{\boldsymbol{\theta}}} &= \frac{\partial U}{\partial \bar{\boldsymbol{\theta}}} = \int_0^{l_0} (EI + GA l^2) \mathbf{c}_{\bar{w}}^T \mathbf{c}_{\bar{w}} \bar{\boldsymbol{\theta}} d\bar{x} + 2 \int_0^{l_0} AE (\bar{\boldsymbol{\theta}}^T \mathbf{B} \bar{\boldsymbol{\theta}} + b_{\bar{u}} \bar{u}_2) b_{\bar{u}} \mathbf{B} \bar{\boldsymbol{\theta}} d\bar{x} \\ &= (EI + GA l^2) \mathbf{C} \bar{\boldsymbol{\theta}} + 2AE (\bar{\boldsymbol{\theta}}^T \mathbf{B} \bar{\boldsymbol{\theta}} + b_{\bar{u}} \bar{u}_2) \mathbf{B} \bar{\boldsymbol{\theta}}, \end{aligned} \quad (26)$$

with

$$\mathbf{C} = \int_0^{l_0} \mathbf{c}_{\bar{w}}^T \mathbf{c}_{\bar{w}} d\bar{x} = \frac{2}{l_0} \begin{bmatrix} 2 & 1 \\ 1 & 2 \end{bmatrix}. \quad (27)$$

It is convenient to split the local matrix  $\bar{\mathbf{k}}_t$  into sub-matrices as

$$\bar{\mathbf{k}}_{(3 \times 3)} = \begin{bmatrix} \bar{k}_{\bar{u}\bar{u}} & \bar{\mathbf{k}}_{\bar{u}\bar{\boldsymbol{\theta}}} \\ \bar{\mathbf{k}}_{\bar{u}\bar{\boldsymbol{\theta}}}^T & \bar{\mathbf{k}}_{\bar{\boldsymbol{\theta}}\bar{\boldsymbol{\theta}}} \end{bmatrix}. \quad (28)$$

The sub-matrices in the above equation have the following form

$$\begin{aligned} \bar{k}_{\bar{u}\bar{u}} &= \frac{\partial \bar{f}_{\bar{u}}}{\partial \bar{u}_2} = EA b_{\bar{u}}, \quad \bar{\mathbf{k}}_{(1 \times 2)} = \frac{\partial \bar{f}_{\bar{u}}}{\partial \bar{\boldsymbol{\theta}}} = 2EA (\bar{\boldsymbol{\theta}}^T \mathbf{B}), \\ \bar{\mathbf{k}}_{(2 \times 2)} &= \frac{\partial \bar{\mathbf{f}}_{\bar{\boldsymbol{\theta}}}}{\partial \bar{\boldsymbol{\theta}}} = 2EA (3 \bar{\boldsymbol{\theta}}^T \mathbf{B} \bar{\boldsymbol{\theta}} + b_{\bar{u}} \bar{u}_2) \mathbf{B} + (EI + GA l^2) \mathbf{C}. \end{aligned} \quad (29)$$

With the derived local internal force vector  $\bar{\mathbf{f}}_{in}$  and the tangent stiffness matrix  $\bar{\mathbf{k}}_t$ , Eqs. (6) and (7) completely define the beam element.

### 3. SOLUTION PROCEDURE

Assembling the derived element nodal force vector  $\mathbf{f}_{in}$  and the tangent stiffness matrix  $\mathbf{k}_t$ , one can construct equilibrium equation which can be written as follows [24]

$$\mathbf{g}(\mathbf{p}, \lambda) = \mathbf{q}_{in}(\mathbf{p}) - \lambda \mathbf{q}_{ef} = \mathbf{0}, \tag{30}$$

where  $\mathbf{p}$  and  $\mathbf{q}_{in}$  are the structural vectors of nodal displacements and nodal internal forces, respectively;  $\mathbf{q}_{ef}$  is the fixed external loading vector, and the scalar  $\lambda$  is a load parameter. Vector  $\mathbf{g}$  in Eq. (30) is known as the residual force vector.

Eq. (30) contains  $n$  unknown nodal displacements, collected in the array  $\mathbf{p}$ . In order to deal with complex behavior such as the limit points and snap-through or snap-back, the arc-length method proposed by Crisfield [26] is adopted herewith. In this method, the load increment  $\lambda$  is considered as an additional unknown, thereby augmenting the  $n$ -dimensional space of displacements to a  $(n + 1)$ -dimensional space of unknowns. An equation, namely the following constraint equation must be added to form a system of  $n + 1$  equations

$$a = (\Delta \mathbf{p}^T \Delta \mathbf{p} + \Delta \lambda \psi \mathbf{q}_{ef}^T \mathbf{q}_{ef}) - \Delta l^2 = 0, \tag{31}$$

where  $\psi$  is a scaling parameter, and  $\Delta l$  is a fixed scalar of the desired intersection between the curve (31) with the equilibrium path. Eqs. (30) and (31) lead to the linearized equation which can be solved for displacements and the load parameter increment by the standard Newton–Raphson based iterative procedure. Details on the arc-length method are described in [24,26].

A convergence criterion is necessary to introduce for the iterative procedure. Here, a criterion based on Euclidean norm of the residual force vector is employed as

$$\|\mathbf{g}\| \leq \varepsilon \|\lambda \mathbf{q}_{ef}\|, \tag{32}$$

with  $\varepsilon$  is the tolerance, chosen by  $10^{-4}$  for all numerical examples given in Section 4.

### 4. NUMERICAL INVESTIGATION

The large displacement behavior of microbeams and microframes subjected to a load or a moment depicted in Fig. 2 is studied in this section. For the convenience of discussion, the following dimensionless parameters for the displacements, the material length

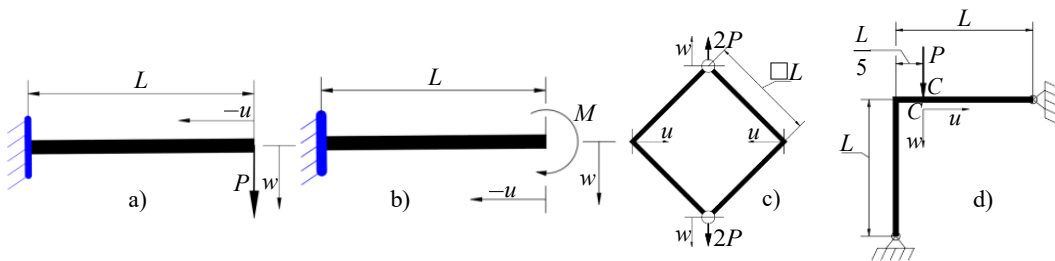


Fig. 2. Microbeams and microframes for numerical investigation

scale parameter and the applied loads are introduced

$$u^* = \frac{u}{L}, \quad w^* = \frac{w}{L}, \quad \eta = \frac{l^2 GA}{EI}, \quad M^* = \frac{ML}{EI}, \quad P^* = \frac{PL^2}{EI}, \quad (33)$$

where  $GA$  and  $EI$  are the shear and bending rigidities, respectively.

#### 4.1. Accuracy and convergence studies

Since the data for large displacements of microbeams and microframes are not available in the literature, the accuracy of the derived formulation is verified herewith by comparing the large displacements of macroframe structure obtained herein by setting  $\eta = 0$  with the published data. To this end, Table 1 lists the tip displacements of the cantilever beam in Fig. 2(a) obtained herein by 8 elements, where the analytical solution derive by Mattiasson [27] and the finite element solutions of Refs. [28,29] are also given. The good agreement between the present result with that of the cited references can be seen from Table 1, regardless of the load level  $P^*$ . The axial and transverse displacements of the square diamond macroframe in Fig. 2(c) obtained by the present formulation are listed in Table 2 for values of the load  $P^*$ . Because of symmetry, only half frame is analyzed, and each beam is discretized herein by using 5 elements. For comparison, the analytical solution of Mattiasson [27] and the finite element result by Nanakorn and Vu [28] are also provided in the table. The good agreement between the present result and that of the cited references is noted from Table 2. In addition, compared to the result based on the total Lagrange element of Ref. [28], the present result is closer to the analytical solution of Mattiasson [27].

Table 1. Comparison of normalized tip displacements of cantilever macrobeam subjected to transverse tip load

Source	$P^*$										
	1	2	3	4	5	6	7	8	9	10	
$u^*$	Ref. [28]	0.0556	0.1567	0.2476	0.3200	0.3773	0.4234	0.4610	0.4925	0.5191	0.5420
	Ref. [29]	- <sup>†</sup>	-	-	0.3289	-	0.4345	-	0.5048	-	0.5550
	Ref. [27]	0.0564	0.1606	0.2544	0.3289	0.3876	0.4346	0.4729	0.5048	0.5318	0.5550
	Present	0.0564	0.1606	0.2543	0.3288	0.3874	0.4342	0.4725	0.5043	0.5311	0.5542
$w^*$	Ref. [28]	0.2995	0.4875	0.5953	0.6613	0.7048	0.7355	0.7583	0.7760	0.7901	0.8017
	Ref. [29]	0.3025	0.4954	0.6058	0.6729	0.7169	0.7478	0.7707	0.7883	0.8024	0.8133
	Ref. [27]	0.3017	0.4935	0.6033	0.6700	0.7138	0.7446	0.7674	0.7850	0.7991	0.8106
	Present	0.3017	0.4934	0.6031	0.6696	0.7133	0.7440	0.7666	0.7841	0.7980	0.8094

<sup>†</sup>: not available.

The convergence of the derived formulation in evaluating large displacements of the microstructure is shown in Figs. 3 and 4 for the cantilever microbeam in Fig. 2(b) and Lee's microframe in Fig. 2(d), respectively. The convergence, as seen from the figures, is achieved by using three elements for the cantilever microbeam and also three elements per beam for Lee's microframe.

Table 2. Comparison of normalized displacements of a square diamond macroframe under tension

Source	$P^*$										
	1	2	3	4	5	6	7	8	9	10	
$u^*$	Ref. [28]	0.1559	0.2489	0.3096	0.3521	0.3837	0.4081	0.4277	0.4437	0.4572	0.4687
	Ref. [27]	0.1396	0.2318	0.2945	0.3394	0.3732	0.3997	0.4210	0.4386	0.4534	0.4660
	Present	0.1389	0.2308	0.2933	0.3375	0.3691	0.3978	0.4166	0.4329	0.4493	0.4646
$w^*$	Ref. [28]	0.1228	0.1723	0.1975	0.2124	0.2221	0.2290	0.2340	0.2380	0.2412	0.2438
	Ref. [27]	0.1125	0.1643	0.1918	0.2084	0.2193	0.2270	0.2328	0.2373	0.2408	0.2438
	Present	0.1127	0.1652	0.1936	0.2107	0.2216	0.2311	0.2370	0.2419	0.2468	0.2515

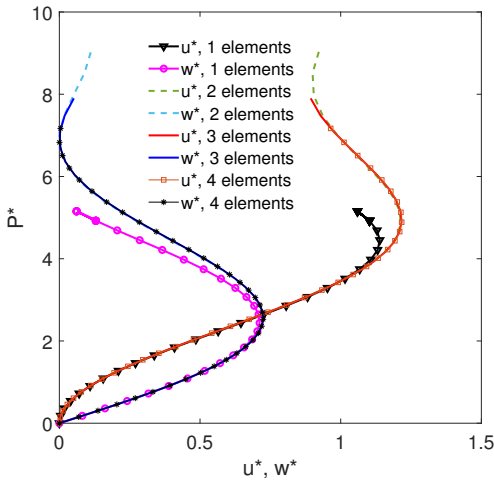


Fig. 3. Convergence of the derived formulation in evaluating tip displacements of cantilever microbeam for  $\eta = 0.1$

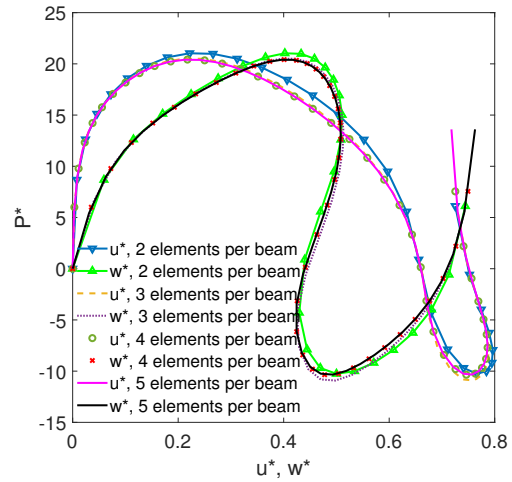


Fig. 4. Convergence of the derived formulation in evaluating displacements at loaded point of Lee's microframe for  $\eta = 0.1$

### 4.2. Cantilever microbeam under a tip load

The size dependent large displacements of the cantilever microbeam under a tip load  $P$  in Fig. 2(a) are studied. In Fig. 5, the load-deflection curves of the microbeam are shown for various values of the material length scale parameter  $\eta$ . As can be seen from the figure, at a given load parameter  $P^*$ , both the tip axial and transverse displacements decrease by increasing the parameter  $\eta$ . Thus, the displacements are overestimated by ignoring the influence of the size effect. The deformed configurations of the microbeams corresponding to  $P^* = 3$  and  $P^* = 10$ , as depicted in Fig. 6, also confirm the significant influence of the material length scale parameter  $\eta$  on the large displacement behavior of the microbeam. Noting that through the convergence of the cantilever microbeam can

be achieved by using 3 elements, 8 elements have been used in computing the beam configurations in the curves Fig. 6 to ensure the smoothness of the curves.

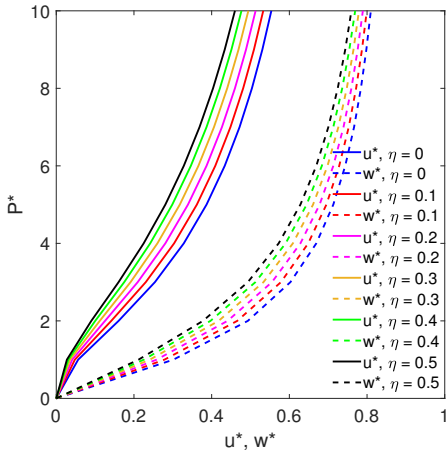


Fig. 5. Load-displacement curves of cantilever microbeam under tip transverse load with various values of length scale parameter  $\eta$

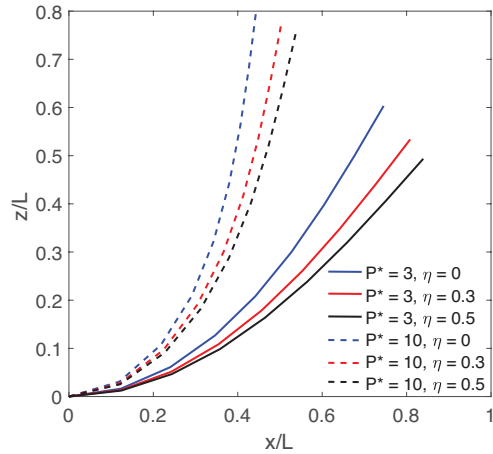


Fig. 6. Deformed configurations of cantilever microbeam under tip transverse load for various values of parameters  $P^*$  and  $\eta$

### 4.3. Roll-up of cantilever microbeam due to a tip moment

A cantilever microbeam under a tip moment  $M$  as depicted in Fig. 2(b) is considered. As reported in as previously shown in [30], the snap-back behavior is occurred for the

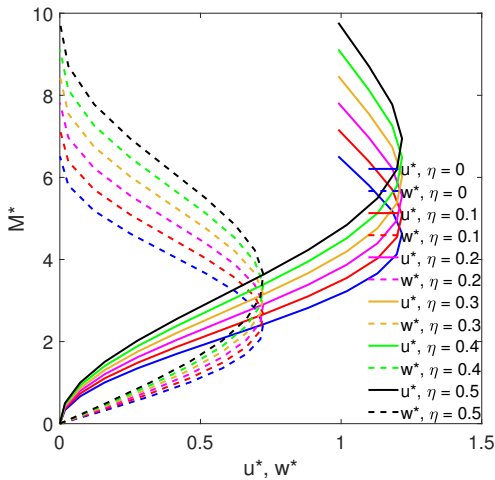


Fig. 7. Effect of material length scale parameter  $\eta$  on load-displacement curves of cantilever microbeam under a tip moment

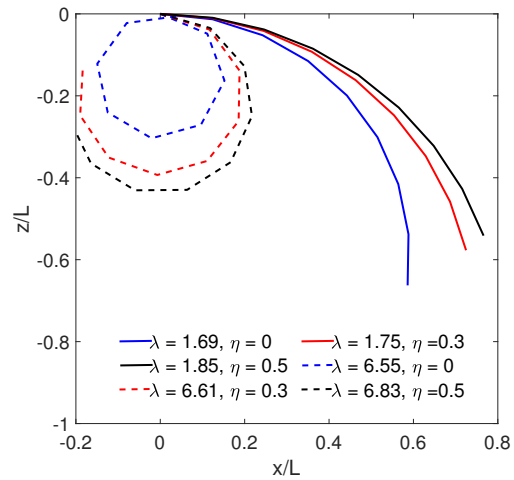


Fig. 8. Deformed configurations of cantilever microbeam under tip moment for various values of parameters  $M^*$  and  $\eta$

microbeam, and thus the arc-length method must be used to trace the equilibrium paths. The effect of the material length scale parameter  $\eta$  on the load-displacement curves of the microbeam is illustrated in Fig. 7. The figure shows a significant influence of the parameter  $\eta$  on the large displacement behavior of the microbeam, and the tip displacements are lower with the presence of the material length scale parameter  $\eta$ . The deformed configurations of the microbeam at the value of the length scale and applied moment parameters are illustrated in Fig. 8 for various values of the scale parameter  $\eta$  and loading parameter  $\lambda$ . The microbeam rolls up a circle by increasing the applied moment.

**4.4. Square diamond microframe in tension**

The size dependent large displacements of a pinned-fixed square diamond microframe loaded in tension with size eff in Fig. 2(c) are studied. The solution of the corresponding macroframe has been analytically derived by Mattiasson [27], and numerically given using a total Lagrangian formulation by Nanakorn and Vu [28]. The load-displacement curves of the microframe obtained herein are shown in Figs. 9 for various values of the material length scale parameter  $\eta$ . Fig. 10 illustrates the deformed configurations of the microframe with  $\eta = 0.1$  and various load parameters. The influence of the material length scale of the large deformation of the microframe can be clearly seen from the figures at various values of the material length scale and the deformed configurations at the value of the material length scale parameter  $\eta = 0.1$  of the microframe are illustrated in Figs. 9 and 10, respectively.

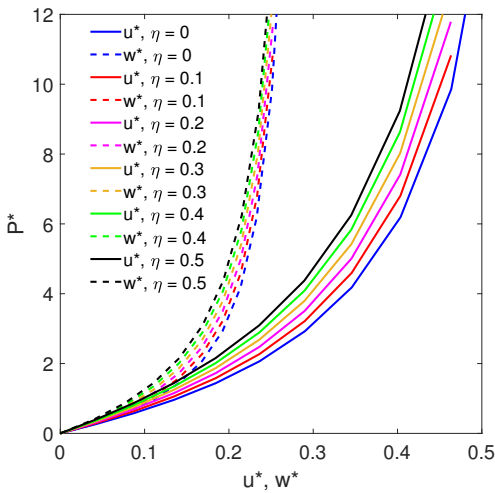


Fig. 9. Effect of the material length scale parameter on load-displacement curves of diamond microframe

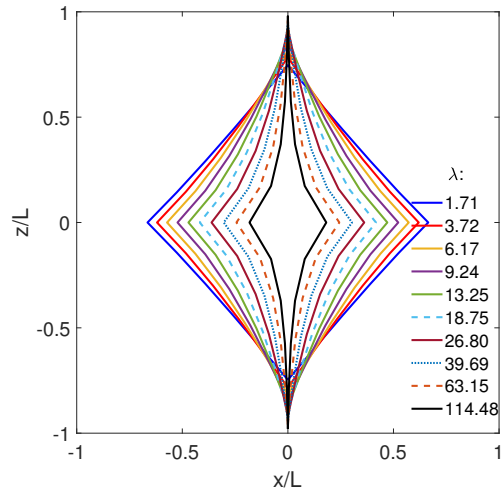


Fig. 10. Deformed configurations of diamond microframe according to various loading parameters ( $\eta = 0.1$ )

#### 4.5. Lee's microframe

The large displacements of an asymmetric microframe under a downward  $P$  in Fig. 2(d) are investigated herewith. The macroframe, also known as Lee's frame in the literature, has been employed by several researchers to test their elements and computer codes [29, 30]. The influence of the size effect and the large displacement behavior of the microframe can be seen from Figs. 11 and 12, where the load-displacement curves and the deformed configurations of the microframes are respectively depicted. Though three elements for each beam are enough to obtain the equilibrium paths in Fig. 11, five elements have been used in analysis to ensure the smoothness of the curves in Fig. 12. The limit load of the microframe, as seen from Fig. 11 is considerably underestimated by ignoring the size effect of the microframe.

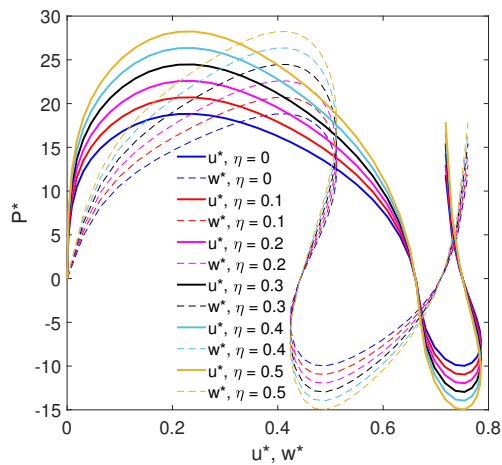


Fig. 11. Load-displacement curves of Lee's microframe for various values of material length scale parameter  $\eta$

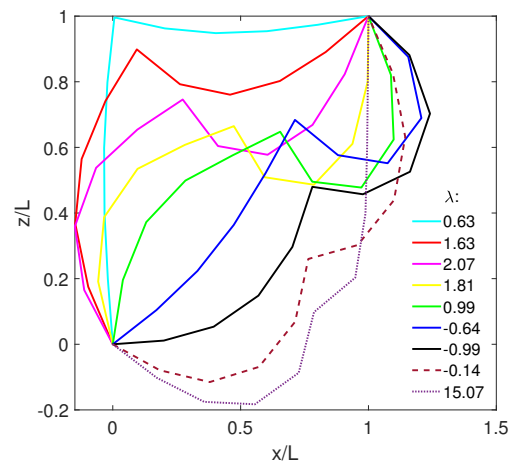


Fig. 12. Deformed configurations of Lee's microframe at for  $\eta = 0.1$  and various values of load parameter  $\lambda$

### 5. CONCLUSIONS

The large displacement behavior of microbeams and microframes has been investigated in this paper using a two-node corotational beam element. To account for the size effect of the micro structures, the MCST was used in conjunction with Euler-Bernoulli beam theory in deriving the internal force vector and tangent stiffness matrix of the beam element. A Newton-Raphson based iterative procedure was employed in combination with the arc-length method to solve the system of nonlinear equations and to trace the load-displacement curves. Various microbeams and microframes have been analyzed to illustrate the behavior of the microbeams and microframes in the large displacement region. The obtained numerical result reveals that the size effect plays an important role in the large displacement behavior of the microstructures, and the displacements are underestimated by ignoring the size effect. The influence of the material length scale parameter

on the large displacements behavior of various microbeams and microframes has been examined in detail and highlighted.

### DECLARATION OF COMPETING INTEREST

The authors declare that they have no known competing financial interests or personal relationships that could have appeared to influence the work reported in this paper.

### FUNDING

This research received no specific grant from any funding agency in the public, commercial, or not-for-profit sectors.

### REFERENCES

- [1] W. Faris and A. H. Nayfeh. Mechanical response of a capacitive microsensor under thermal load. *Communications in Nonlinear Science and Numerical Simulation*, **12**, (5), (2007), pp. 776–783. <https://doi.org/10.1016/j.cnsns.2005.06.006>.
- [2] M. I. Younis. *MEMS linear and nonlinear statics and dynamics*, Vol. 20. Springer Science & Business Media, (2011). <https://doi.org/10.1007/978-1-4419-6020-7>.
- [3] B. Choi and E. G. Lovell. Improved analysis of microbeams under mechanical and electrostatic loads. *Journal of Micromechanics and Microengineering*, **7**, (1), (1997), pp. 24–29. <https://doi.org/10.1088/0960-1317/7/1/005>.
- [4] E. M. Abdel-Rahman, M. I. Younis, and A. H. Nayfeh. Characterization of the mechanical behavior of an electrically actuated microbeam. *Journal of Micromechanics and Microengineering*, **12**, (6), (2002), pp. 759–766. <https://doi.org/10.1088/0960-1317/12/6/306>.
- [5] E. M. Abdel-Rahman and A. H. Nayfeh. Secondary resonances of electrically actuated resonant microsensors. *Journal of Micromechanics and Microengineering*, **13**, (3), (2003), pp. 491–501. <https://doi.org/10.1088/0960-1317/13/3/320>.
- [6] M. I. Younis, E. M. Abdel-Rahman, and A. Nayfeh. A reduced-order model for electrically actuated microbeam-based MEMS. *Journal of Microelectromechanical Systems*, **12**, (5), (2003), pp. 672–680. <https://doi.org/10.1109/JMEMS.2003.818069>.
- [7] M. I. Younis and A. H. Nayfeh. A study of the nonlinear response of a resonant microbeam to an electric actuation. *Nonlinear Dynamics*, **31**, (1), (2003), pp. 91–117. <https://doi.org/10.1023/A:1022103118330>.
- [8] S. Chatterjee and G. Pohit. A large deflection model for the pull-in analysis of electrostatically actuated microcantilever beams. *Journal of Sound and Vibration*, **322**, (4-5), (2009), pp. 969–986. <https://doi.org/10.1016/j.jsv.2008.11.046>.
- [9] D. C. C. Lam, F. Yang, A. C. M. Chong, J. Wang, and P. Tong. Experiments and theory in strain gradient elasticity. *Journal of the Mechanics and Physics of Solids*, **51**, (8), (2003), pp. 1477–1508. [https://doi.org/10.1016/S0022-5096\(03\)00053-X](https://doi.org/10.1016/S0022-5096(03)00053-X).
- [10] M. H. Kahrobaiyan, M. Asghari, M. Rahaeifard, and A. A nonlinear strain gradient beam formulation. *International Journal of Engineering Science*, **49**, (11), (2011), pp. 1256–1267. <https://doi.org/10.1016/j.ijengsci.2011.01.006>.
- [11] F. A. C. M. Yang, A. C. M. Chong, D. C. C. Lam, and P. Tong. Couple stress based strain gradient theory for elasticity. *International Journal of Solids and Structures*, **39**, (10), (2002), pp. 2731–2743. [https://doi.org/10.1016/S0020-7683\(02\)00152-X](https://doi.org/10.1016/S0020-7683(02)00152-X).

- [12] H. Mohammadi and M. Mahzoon. Thermal effects on postbuckling of nonlinear microbeams based on the modified strain gradient theory. *Composite Structures*, **106**, (2013), pp. 764–776. <https://doi.org/10.1016/j.compstruct.2013.06.030>.
- [13] W. Xia, L. Wang, and L. Yin. Nonlinear non-classical microscale beams: static bending, postbuckling and free vibration. *International Journal of Engineering Science*, **48**, (12), (2010), pp. 2044–2053. <https://doi.org/10.1016/j.ijengsci.2010.04.010>.
- [14] M. Asghari, M. H. Kahrobaiyan, and M. T. Ahmadian. A nonlinear Timoshenko beam formulation based on the modified couple stress theory. *International Journal of Engineering Science*, **48**, (12), (2010), pp. 1749–1761. <https://doi.org/10.1016/j.ijengsci.2010.09.025>.
- [15] M. Asghari, M. H. Kahrobaiyan, M. Nikfar, and M. T. Ahmadian. A size-dependent nonlinear Timoshenko microbeam model based on the strain gradient theory. *Acta Mechanica*, **223**, (6), (2012), pp. 1233–1249. <https://doi.org/10.1007/s00707-012-0625-0>.
- [16] S. Ramezani. A micro scale geometrically non-linear Timoshenko beam model based on strain gradient elasticity theory. *International Journal of Non-Linear Mechanics*, **47**, (8), (2012), pp. 863–873. <https://doi.org/10.1016/j.ijnonlinmec.2012.05.003>.
- [17] B. Akgöz and Ö. Civalek. Buckling analysis of functionally graded microbeams based on the strain gradient theory. *Acta Mechanica*, **224**, (9), (2013), pp. 2185–2201. <https://doi.org/10.1007/s00707-013-0883-5>.
- [18] B. Akgöz and Ö. Civalek. A novel microstructure-dependent shear deformable beam model. *International Journal of Mechanical Sciences*, **99**, (2015), pp. 10–20. <https://doi.org/10.1016/j.ijmecsci.2015.05.003>.
- [19] Y.-G. Wang, W.-H. Lin, and N. Liu. Nonlinear bending and post-buckling of extensible microscale beams based on modified couple stress theory. *Applied Mathematical Modelling*, **39**, (1), (2015), pp. 117–127. <https://doi.org/10.1016/j.apm.2014.05.007>.
- [20] R. Ansari, M. F. Shojaei, V. Mohammadi, R. Gholami, and M. A. Darabi. Buckling and post-buckling behavior of functionally graded Timoshenko microbeams based on the strain gradient theory. *Journal of Mechanics of Materials and Structures*, **7**, (10), (2013), pp. 931–949. <https://doi.org/10.2140/jomms.2012.7.931>.
- [21] R. Ansari, M. F. Shojaei, and R. Gholami. Size-dependent nonlinear mechanical behavior of third-order shear deformable functionally graded microbeams using the variational differential quadrature method. *Composite Structures*, **136**, (2016), pp. 669–683. <https://doi.org/10.1016/j.compstruct.2015.10.043>.
- [22] F. Dadgar-Rad and A. Beheshti. A nonlinear strain gradient finite element for microbeams and microframes. *Acta Mechanica*, **228**, (5), (2017), pp. 1941–1964. <https://doi.org/10.1007/s00707-017-1798-3>.
- [23] M. A. Attia and S. A. Mohamed. Nonlinear thermal buckling and postbuckling analysis of bidirectional functionally graded tapered microbeams based on Reddy beam theory. *Engineering with Computers*, (2020), pp. 1–30. <https://doi.org/10.1007/s00366-020-01080-1>.
- [24] M. A. Crisfield. *Nonlinear finite element analysis of solids and structures. Volume 1: Essentials*. Wiley, New York, (1991).
- [25] D. K. Nguyen. A Timoshenko beam element for large displacement analysis of planar beams and frames. *International Journal of Structural Stability and Dynamics*, **12**, (06), (2012). <https://doi.org/10.1142/S0219455412500484>.
- [26] M. A. Crisfield. A fast incremental/iterative solution procedure that handles “snap-through”. *Computers & Structures*, **13**, (1981), pp. 55–62. [https://doi.org/10.1016/0045-7949\(81\)90108-5](https://doi.org/10.1016/0045-7949(81)90108-5).

- [27] K. Mattiasson. Numerical results from large deflection beam and frame problems analysed by means of elliptic integrals. *International Journal for Numerical Methods in Engineering*, **17**, (1), (1981), pp. 145–153. <https://doi.org/10.1002/nme.1620170113>.
- [28] P. Nanakorn and L. N. Vu. A 2D field-consistent beam element for large displacement analysis using the total Lagrangian formulation. *Finite Elements in Analysis and Design*, **42**, (14-15), (2006), pp. 1240–1247. <https://doi.org/10.1016/j.finel.2006.06.002>.
- [29] D. K. Nguyen, B. S. Gan, and T. H. Trinh. Geometrically nonlinear analysis of planar beam and frame structures made of functionally graded material. *Structural Engineering and Mechanics: An International Journal*, **49**, (6), (2014), pp. 727–743. <https://doi.org/10.12989/sem.2014.49.6.727>.
- [30] K. M. Hsiao and F. Y. Hou. Nonlinear finite element analysis of elastic frames. *Computers & Structures*, **26**, (4), (1987), pp. 693–701. [https://doi.org/10.1016/0045-7949\(87\)90016-2](https://doi.org/10.1016/0045-7949(87)90016-2).